RSC Advances

PAPER

View Article Online
View Journal | View Issue

Cite this: *RSC Adv.*, 2025, **15**, 27334

Dual deep red and far red emitting Cr-doped garnet-perovskite based phosphors with excellent responsiveness to P_{fr} for plant growth LED lighting

Khuat Thi Thu,[a] Nguyen Tu, *[a] Do Quang Trung,[a] Nguyen Van Du,[a] Nguyen Van Quang,[b] Ta Ngoc Bach,[c] Nghiem Thi Ha Lien,[d] Nguyen Duy Hung,[e] Dao Xuan Viet,[e] Pham Thi Lan Huong,[f] Tong Thi Hao Tam,[g] Nguyen Minh Hieu,[h] Manh Trung Tran[h] and Pham Thanh Huy[h]

Received 26th May 2025
Accepted 25th July 2025

DOI: 10.1039/d5ra03696h

rsc.li/rsc-advances

Cr^{3+}-activated phosphors, with their $3d^3$ electronic configuration, efficiently absorb blue/violet light and emit deep to far-red wavelengths, perfectly matching the optimal absorption bands for plant growth. In this work, we report the synthesis of $Y_3Al_5O_{12}$–$YAlO_3$:1.3%Cr^{3+} (YAG–YAP:Cr^{3+}) phosphors exhibiting a broad emission spanning deep to far-red light, closely aligned with the far-red phytochrome (P_{fr}) absorption spectrum in plants. The optimized sample, sintered at 1600 °C for 5 hours, demonstrates outstanding photoluminescence performance, including an exceptional activation energy of 0.34 eV, a long luminescence lifetime of 1.86 ms, perfect color purity (100%), and a high internal quantum efficiency of 74.9%. A prototype plant-growth LED was fabricated by coating this phosphor onto a 415 nm violet LED chip, achieving a strong spectral overlap (65% SR index) with the P_{fr} absorption band. These results demonstrate that YAG–YAP:Cr^{3+} phosphors are highly promising candidates for efficient, targeted far-red LEDs tailored for enhanced plant cultivation.

1. Introduction

Environmental challenges such as extreme weather and pest outbreaks increasingly threaten outdoor agriculture, driving the critical need for indoor cultivation in modern horticulture.[1] As a result, extensive research has been conducted to address this issue.[2,3] Light plays a vital role in many aspects of our lives. For instance, certain organic optical materials that emit in the near-infrared region have been developed and are used in the treatment of various diseases.[4,5] Notably, light is also a fundamental factor in plant growth, with key pigments including chlorophyll A, chlorophyll B, red phytochrome (P_r), and far-red phytochrome (P_{fr}), sensitive to blue (400–500 nm), red (620–690 nm), and far-red (700–740 nm) wavelengths.[6–8] These wavelengths are essential for photosynthesis, phototropism, and photomorphogenesis,[8,9] making tailored light sources vital for effective indoor farming. Light-emitting diodes (LEDs) have become preferred plant light sources due to their brightness, compactness, longevity, energy efficiency, low heat, and tunable spectra.[2,3,8–11] Yet, high costs, thermal instability, and inconsistent drive voltages limit their broader application.[8,10] Phosphor-converted LEDs (pc-LEDs), which combine phosphors with excitation sources, offer a promising alternative.[12] The growing demand for specialized blue, red, and far-red lighting to support various plant growth stages has fueled research into far-red LEDs, specifically targeting the P_{fr} absorption region.[13]

Notable Cr^{3+}-doped phosphors that have been investigated include $ZnGa_2O_4$:Cr^{3+} (emission wavelength, λ_{em} ~710 nm),[11] $SrMgAl_{10}O_{17}$:Cr^{3+} (λ_{em} ~695 nm),[12] Na_3AlF_6:Cr^{3+} (λ_{em} ~720 nm),[14] $ZnAl_2O_4$:Cr^{3+} (λ_{em} ~698 nm),[6] $BaMgAl_{10}O_{17}$:Cr^{3+} (λ_{em} ~696 and 726 nm).[15] The Cr^{3+} ions are widely recognized as an effective activator for deep to far-red emission due to its $3d^3$ electron coordination, which enables absorption of blue and/or violet light and emission in the deep to far-red region. Thus, Cr^{3+} ions, with their $3d^3$ configuration, efficiently absorb blue/violet light and emit deep to far-red light, aligning closely with the plant P_{fr} spectrum, making them ideal activators for far-red phosphors.[11,12,14] In addition, the host lattice plays

[a]Faculty of Fundamental Science, Phenikaa University, Yen Nghia, Ha-Dong District, Hanoi 12116, Vietnam. E-mail: tu.nguyen@phenikaa-uni.edu.vn
[b]Department of Chemistry, Hanoi Pedagogical University 2, Phuc Yen, Vinh Phuc, Vietnam
[c]Institute of Materials Science – Vietnam Academy of Science and Technology, Cau Giay District, Hanoi 10000, Vietnam
[d]Institute of Physics – Vietnam Academy of Science and Technology, 10 Dao Tan, Ba Dinh District, Hanoi 10000, Vietnam
[e]Faculty of Electronic Materials and Components, School of Materials Science and Engineering, Hanoi University of Science and Technology (HUST), 01 Dai Co Viet Street, Hanoi 10000, Vietnam
[f]Faculty of Biotechnology, Chemistry and Environmental Engineering, Phenikaa University, Hanoi 12116, Vietnam
[g]Faculty of Information Technology, College of Technology, National Economics University (NEU), Giai Phong Street, Hanoi 10000, Vietnam
[h]Faculty of Materials Science and Engineering, Phenikaa School of Engineering, Phenikaa University, Yen Nghia, Ha-Dong District, Hanoi 12116, Vietnam

a critical role in determining the optical properties of phosphors.[16–18] $Y_3Al_5O_{12}$ (YAG) garnet, a wide-bandgap material, is widely used in commercial white LEDs due to its excellent physical, chemical, and mechanical stability.[19,20] Although Cr^{3+}-doped YAG phosphors emit intense deep-red light (650–750 nm, peak at ~693 nm) for deep-red phytochrome applications,[19,21–25] their limited far-red coverage reduces efficiency in plant-growth LEDs.[26–28] In contrast, $YAlO_3$ (YAP):Cr^{3+} phosphors exhibit the strong far-red region (670–800 nm, peak ~745 nm),[29,30] closely aligning with the P_{fr} absorption spectrum in plants. Therefore, combining YAG and YAP lattices in Cr^{3+}-doped YAG–YAP composite phosphors offers a promising strategy to broaden emission across the deep-to-far-red range, enhancing compatibility with plant phytochrome responses.

In this work, $Y_3Al_5O_{12}$–$YAlO_3$:Cr^{3+} phosphors emitting across the deep to far-red region were synthesized using a simple solid-state reaction method. The effects of heat treatment and Cr^{3+} concentration on the crystal structure, morphology, and optical properties were investigated. The occupation of Cr^{3+} ions at octahedral sites, along with decay time, color purity, and thermal stability, was analyzed. A prototype LED, fabricated by combining YAG–YAP:Cr^{3+} with a 415 nm chip, exhibited broadband emission aligned with the P_{fr} absorption spectrum of plants. In addition, the internal quantum efficiency (IQE) of the phosphor was evaluated in detail.

2. Experimental

2.1. Materials

Yttrium(III) oxide (Y_2O_3, 99.9%), chromium(III) chloride hexahydrate ($CrCl_3 \cdot 6H_2O$, 99.9%), and aluminium oxide (Al_2O_3, 99.9%) were procured from Sigma-Aldrich and used as received. Deionized water was also utilized.

2.2. Synthesis of $Y_3Al_5O_{12}$–$YAlO_3$:Cr^{3+} phosphor and the LEDs packaging process

YAG–YAP:x% Cr^{3+} phosphors (x = 0.2–3.0) were synthesized using a simple solid-state reaction technique. Initially, Y_2O_3, Al_2O_3, and $CrCl_3 \cdot 6H_2O$ in varying molar ratios were dispersed in 75 mL of deionized water and stirred magnetically for 30 minutes. The mixture was then heated at 200 °C under ambient conditions until the water completely evaporated. The resulting dry powder was finely ground using a high-energy planetary ball mill at 200 rpm for 30 minutes. Finally, the powder was annealed in air at temperatures ranging from 1000 to 1600 °C to synthesize the YAG–YAP:Cr^{3+} phosphors.

The optimized YAG–YAP:Cr^{3+} phosphors were coated onto a 415 nm violet LED chip to fabricate a plant-growth LED. The packaging process followed the procedure detailed in our previous studies.[6,31]

2.3. Characterization

The surface characteristics and elemental distribution were investigated using field emission scanning electron microscopy (FE-SEM, JEOL JSM-7600F). High-resolution structural analysis was conducted using a JEM-2500SE (JEOL) transmission electron microscope (TEM) operated at an accelerating voltage of 200 kV. The structural properties of all samples were analyzed using X-ray diffraction (Siemens D6000) with Cu K_α radiation (λ = 0.154 nm), employing precise step increments of 0.02° across the 2θ range of 15–75°. The Fourier transform-infrared spectroscopy (FT-IR, Spectrum Two, Perkin Elmer-USA) was employed to analyze the chemical bonds within the materials. The energy levels associated with Al, Y, O, and Cr were examined using a Kα X-ray photoelectron spectrometer system (XPS, Thermo Scientific, USA). The photoluminescence (PL) and excitation photoluminescence (PLE) spectra of all samples were analyzed using a fluorescence spectrophotometer (NanoLog, Horiba) powered by a 450 W Xenon lamp. Finally, the optical properties of the LED devices were assessed using a Gamma Scientific GS-1290 spectroradiometer (RadOMA). All measurements were conducted under ambient conditions.

3. Results and discussions

3.1. XRD pattern, FESEM image, and EDS spectrum

Fig. 1a presents the XRD pattern of $Y_3Al_5O_{12}$–$YAlO_3$:1.3% Cr^{3+} phosphor synthesized at 1600 °C for 5 h in air, revealing two main phases of $Y_3Al_5O_{12}$ (YAG) and $YAlO_3$ (YAP). The major characteristic peaks at the 2θ angle of 18.07°, 20.84°, 27.73°, 29.60°, 33.34°, 35.15°, 36.56°, 38.22°, 41.13°, 42.63°, 46.60°, 52.70°, 55.06°, 56.18°, 57.30°, 61.70°, 69.96°, and 71.98° correspond to (211), (220), (321), (400), (420), (332), (422), (431), (521), (440), (532), (444), (640), (721), (642), (800), (840), and (842) planes of the $Y_3Al_5O_{12}$ cubic structure (JCPDS No 33-0040).[32,33] The remaining peaks are attributed to the orthorhombic $YAlO_3$ phase (JCPDS No 33-0041).[34] Fig. 1b presents the Rietveld refinement analysis of the same sample, confirming the coexistence of YAG and YAP phases. The low value of χ^2 (~1.58) confirms excellent agreement between the experimental and calculated patterns, validating the structural model. Fig. 1c displays the XRD patterns of YAG–YAP:1.3% Cr^{3+} phosphors synthesized at various temperatures ranging from 1000 to 1600 °C. The formation of YAG and YAP phases begins at 1300 °C, with improved crystallinity observed at higher annealing temperatures. Fig. 1d illustrates the XRD patterns of YAG–YAP:x% Cr^{3+} (x = 0.2–3.0) phosphors annealed at 1600 °C. A noticeable shift of the (211) peak toward lower 2θ values with increasing Cr^{3+} contents suggests the incorporation of larger Cr^{3+} ions in place of smaller host ions within the YAG–YAP lattices.

The difference between the host ionic radius of the host ion and that of the dopant (D_r) can be estimated using eqn (1):[35]

$$D_r = \frac{|R_m(CN) - R_d(CN)|}{R_m(CN)} \times 100\% \quad (1)$$

where CN is the coordination number, R_m(CN) and R_d(CN) are the ionic radii of the host and dopant ions, respectively. For Cr^{3+} ions (CN = 6, r = 0.62 Å), the calculated D_r values when substituting Al^{3+} ions in tetrahedral (CN = 4, r = 0.39 Å), octahedral (CN = 6, r = 0.535 Å) and Y^{3+} sites (CN = 8, r = 1.019 Å) are 58.97%, 15.88% and 39.15%, respectively. It has been reported that substitutional doping is likely to occur when the D_r

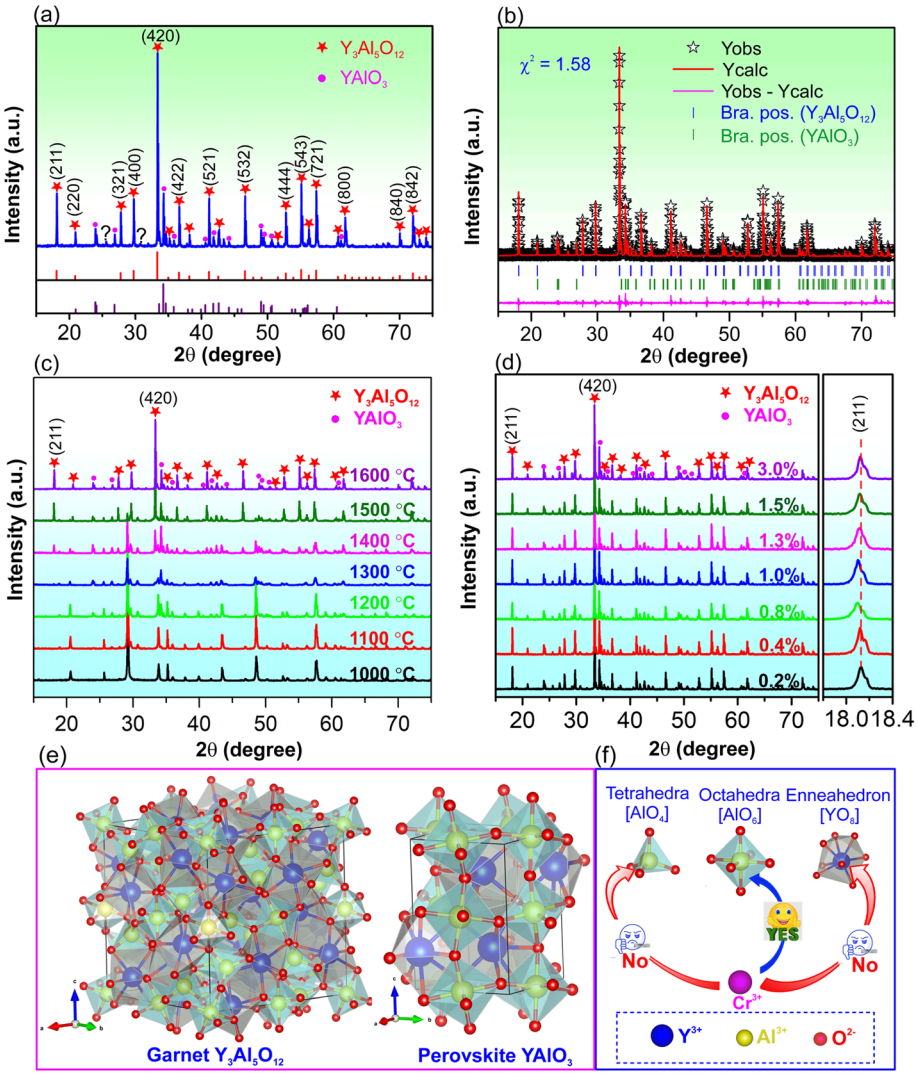

Fig. 1 (a) XRD pattern, (b) Rietveld refinement of the YAG–YAP:1.3% Cr^{3+} sample. (c & d) XRD patterns of YAG–YAP:Cr^{3+} annealed at different temperatures in the range of 1000–1600 °C and doped at various concentrations of Cr^{3+}. (e) Graphical representation of the $Y_3Al_5O_{12}$ garnet and $YAlO_3$ perovskite structures. (f) [AlO_4] tetrahedra, [AlO_6] octahedra, and [YO_8] sites occupied by constituent Cr^{3+} ions.

value does not exceed 30%.[36] This suggests that Cr^{3+} ions preferentially substitute Al^{3+} ions in [AlO_6] octahedral sites, rather than in [AlO_4] tetrahedra or [YO_8] enneahedral sites within the YAG and YAP lattices. These findings are further supported by the crystallographic model generated using VESTA sorfware, as depicted in Fig. 1e, which illustrates the substitution of smaller Al^{3+} ions (CN = 6, r = 0.535 Å) by the larger Cr^{3+} ions (CN = 6, r = 0.62 Å) within the YAG and YAP lattices (Fig. 1f).

To confirm it, Rietveld refinement was performed on YAG–YAP:x% Cr^{3+} (x = 0.2–3.0) samples, with the results shown in Fig. 2. The refined lattice parameters and unit cell volumes of (V_1) and YAP (V_2) for YAG–YAP:x% Cr^{3+} samples annealed at 1600 °C for 5 hours in air are summarized in Table 1. The consistently low χ^2 values confirm excellent agreement between the experimental data and the calculated patterns. As shown in Table 1, both V_1 and V_2 increase progressively with rising Cr^{3+} concentration, indicating the substitution of smaller Al^{3+} ions by larger Cr^{3+} ions within the YAG–YAP lattices.

Fig. 3a–f show the FESEM image of YAG–YAP:1.3% Cr^{3+} samples annealed at various temperatures ranging from 1000 to 1600 °C for 5 hours in air. A clear increase in particle size is observed with rising annealing temperature, likely due to the agglomeration of smaller particles.[6,37] At 1600 °C, the particles grow to sizes of approximately 1–2 μm, which is well-suited for phosphor-converted LED (pc-LED) applications.[38] The EDS spectrum in Fig. 3g confirms the presence of Y (16.36%), Al (13.63%), O (69.90%), and Cr (0.11%) without detectable impurities, indicating high sample purity. Furthermore, EDS elemental mapping (Fig. 3h) reveals a uniform distribution of all constituent elements within the YAG–YAP:1.3% Cr^{3+} phosphor.

3.2. HRTEM analysis

To confirm the presence of both YAG and YAP phases in the sample, TEM, selected area electron diffraction (SAED), and

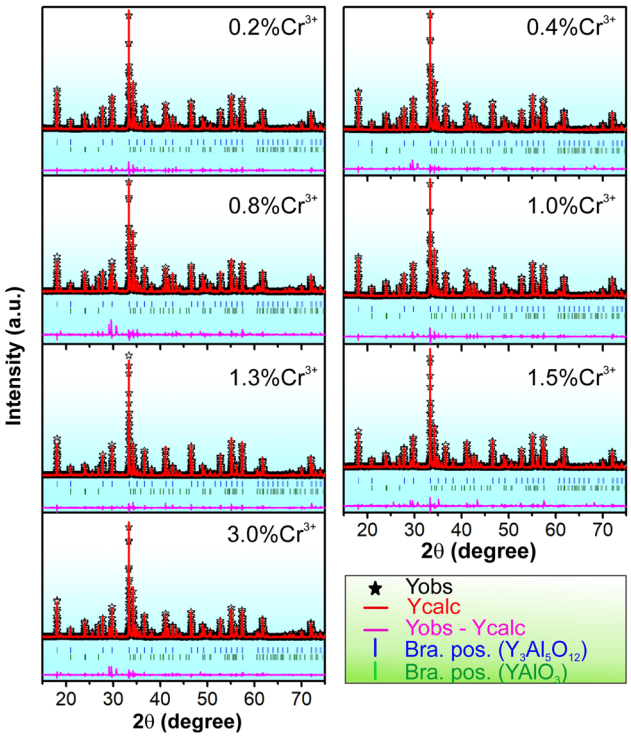

Fig. 2 The Rietveld refinement analysis for YAG–YAP:x% Cr^{3+} (x = 0.2–3.0) samples annealed at 1600 °C for 5 hours in air.

Table 1 Lattice parameters and unit cell volumes of $Y_3Al_5O_{12}$ (V_1) and $YAlO_3$ (V_2) in the YAG–YAP:x% Cr^{3+} (x = 0.2–3.0) phosphors annealed at 1600 °C for 5 hours in air

	$Y_3Al_5O_{12}$		$YAlO_3$				
% Cr^{3+}	$a = b = c$	V_1	a	b	c	V_2	χ^2
0.2	12.0093	1732.057	5.1803	5.3274	7.3720	203.449	2.39
0.4	12.0095	1732.109	5.1806	5.3274	7.3720	203.463	1.65
0.6	12.0103	1732.454	5.1805	5.3291	7.3724	203.536	2.52
1.0	12.0108	1732.700	5.1812	5.3310	7.3743	203.691	2.50
1.3	12.0108	1732.700	5.1812	5.3310	7.3743	203.691	1.58
1.5	12.0110	1732.762	5.1812	5.3311	7.3743	203.692	1.48
3.0	12.0126	1733.450	5.1829	5.3354	7.3779	203.825	2.81

high-resolution TEM (HRTEM) analyses were conducted. The TEM image (Fig. 4a) reveals a polycrystalline microstructure. The SAED pattern (Fig. 4b) exhibits distinct diffraction rings, which can be indexed to the cubic YAG and orthorhombic YAP structures. Detailed examination of the yellow-boxed regions in Fig. 4c confirms the presence of well-defined polycrystalline domains. Fast Fourier Transform (FFT) patterns from the red-boxed areas (Fig. 4d and f) exhibit symmetrical diffraction spots, while the corresponding inverse FFT (IFFT) images (Fig. 4e and g) reveal a well-ordered atomic lattice. The observed interplanar spacings of 0.269 nm and 0.250 nm correspond to the (402) and (210) planes of YAG and YAP, respectively.[39,40] These results provide clear structural evidence for the coexistence of YAG and YAP phases, in strong agreement with the XRD analysis.

3.3. XPS spectra investigation

Fig. 5 illustrates the XPS spectra of YAG–YAP:1.3% Cr^{3+} phosphors synthesized at 1600 °C for 5 h in air. The full-range scan (Fig. 5a) reveals characteristic peaks corresponding to Y, Al, O, and Cr, with no detectable impurities apart from the C 1s signal at 284.6 eV, attributed to surface contamination (Fig. 5b). The high-resolution Y 3d spectrum (Fig. 5c) shows two spin–orbit doublets at 156.7/158.8 eV and 157.4/159.4 eV, corresponding to Y–O bonds in the YAG and YAP lattices, respectively.[41,42] The Al 2p spectrum (Fig. 5d) reveals four deconvoluted peaks at 73.2, 73.6, 73.9, and 74.6 eV. Peaks at 73.2 and 73.9 eV (Al $2p_{3/2}$ and Al $2p_{1/2}$) are assigned to Al–O bonds in the YAG structure, while those at 73.6 and 74.6 eV correspond to Al–O bonds in the YAP phase.[43,44] In the O 1s spectrum (Fig. 5e), three peaks at 529.9, 531.4, and 532.9 eV are observed, attributed to metal–oxygen bonds (Y–O and Al–O) and adsorbed oxygen species.[43,44] The Cr 2p spectrum (Fig. 5f) shows two prominent peaks at 577.1 and 585.9 eV, corresponding to Cr $2p_{3/2}$ and Cr $2p_{1/2}$, respectively. The observed spin–orbit splitting of 8.8 eV confirms the Cr^{3+} oxidation state.[45] Collectively, the XPS analysis confirms the successful incorporation of Cr^{3+} ions into both YAG and YAP host lattices. Additional details, including binding energies, full width at half maximum (FWHM), and spin–orbit splitting values, are provided in Table S1 of the SI. Moreover, the presence of Al–O and Y–O bonds is further corroborated by the FTIR results shown in Fig. S1 of the SI.

3.4. Photoluminescence and excitation photoluminescence

Fig. 6a describes the PLE spectrum measured at 695 nm of the YAG–YAP:1.3% Cr^{3+} phosphors sintered at 1600 °C for 5 h. The PLE spectrum exhibits three broad excitation bands peaking at approximately 275, 423, and 602 nm, corresponding to the O^{2-}–Cr^{3+} charge transfer band (CTB), and the $^4A_2 \rightarrow {}^4T_1$ (F), and $^4A_2 \rightarrow {}^4T_2$ of Cr^{3+} ions, respectively.[19,21–25] The PL spectrum (Fig. 6b) exhibits a broad 620–800 nm emission. This emission is resolved into two distinct bands in Fig. 6c: a deep-red peak at 695 nm attributed to the $^2E \rightarrow {}^4A_2$ transition of Cr^{3+} in the YAG lattice,[15,25] and a far-red peak at 733 nm from the same transition in the YAP lattice.[29] The energy-level splitting of Cr^{3+} ions is further explained using the Tanabe–Sugano diagram, which relates the splitting to the crystal field strength, defined by the D_q/B ratio, where D_q is the ligand-field splitting parameter and B is the Racah parameter.[15] These values are derived from the excitation bands in Fig. 6a using the following eqn (2)–(4):[6,46]

$$D_q = \frac{E(^4A_2 - {}^4T_2)}{10} \quad (2)$$

$$x = \frac{E(^4A_2 - {}^4T_2(F)) - E(^4A_2 - {}^4T_2)}{D_q} \quad (3)$$

$$\frac{D_q}{B} = \frac{15(x-8)}{x^2 - 10x} \quad (4)$$

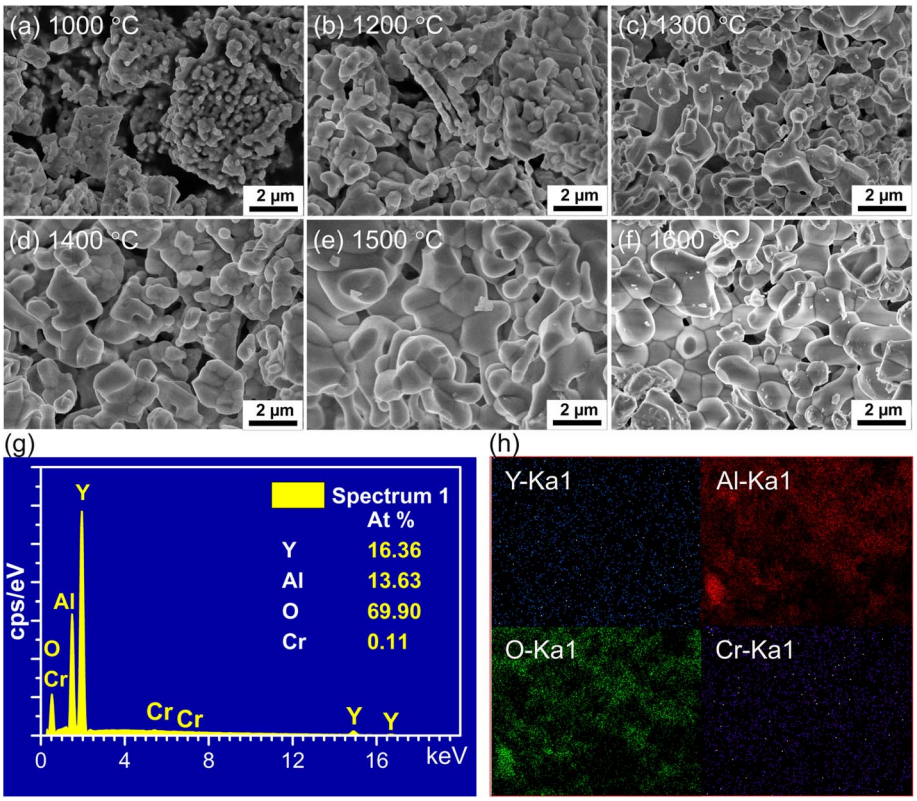

Fig. 3 (a–f) FESEM images of the YAG–YAP:1.3% Cr^{3+} sample annealed at different temperatures in the range of 1000–1600 °C (g & h) EDS and EDS mapping spectra of the YAG–YAP:1.3% Cr^{3+} sample annealed at 1600 °C.

As shown in Fig. 6d, the estimated D_q/B value of 3.2 (>2.3) confirms that Cr^{3+} ions occupy [AlO_6] octahedral sites in a strong crystal field,[47] with the lowest excited state being the ^2E level. This leads to PL spectra featuring sharp R-line transitions and phonon sidebands.[15] Thus, the absorption and emission mechanisms of Cr^{3+} in YAG and YAP are illustrated in Fig. 6e. Fig. 6f presents the PL spectra of YAG–YAP:1.3% Cr^{3+} annealed at 1000–1600 °C for 5 h. While the spectral shape remains consistent, PL intensity increases with temperature, peaking at 1600 °C, which is attributed to enhanced phase formation and improved Cr^{3+} diffusion into [AlO_6] sites.[15,47] Fig. 6g shows PL spectra (λ_{ex} = 423 nm) of YAG–YAP:x% Cr^{3+} (x = 0.2–3.0) samples annealed at 1600 °C. Emission intensity rises with Cr^{3+} content up to 1.3% due to increased emission centers,[15,48] but decreases at higher concentrations from concentration quenching.[49,50] At >1.3%, Cr^{3+} ions are closer than the critical distance (R_c), enabling non-radiative energy transfer.[13,48] PLE spectra in Fig. S2 of the SI further confirm that the YAG–YAP:1.3% Cr^{3+} sample annealed at 1600 °C yields the highest excitation and emission intensities.[51]

3.5. Color purity, lifetime, thermal stability, and internal quantum efficiency of phosphors

The chromaticity coordinates of the YAG–YAP:x% Cr^{3+} (x = 0.2–3.0) phosphors synthesized at 1600 °C were calculated using Color Calculator software, with results summarized in Fig. 7a and Table 2. All coordinates fall beyond the boundary of the red region in the CIE 1931 chromaticity diagram, indicating excellent red color purity. The color purity was quantitatively evaluated using eqn (5):[52]

$$\text{Color purity} = \frac{\sqrt{(x-x_i)^2+(y-y_i)^2}}{\sqrt{(x_d-x_i)^2+(y_d-y_i)^2}} \quad (5)$$

Here, (x, y) are the chromaticity coordinates of the phosphor emission, (x_i, y_i) = (0.3333, 0.3333) represent the white illuminant,[52] and (x_d, y_d) correspond to the dominant wavelength extracted from the emission spectra in Fig. 6g. As shown in Fig. 7a and Table 2, all samples exhibit a calculated color purity of 100%, confirming their superior color purity.[6,37,52]

Fig. 7b shows the PL decay curves of the YAG–YAP:x% Cr^{3+} (x = 0.2–1.5%) samples under 423 nm excitation. These samples, annealed at 1600 °C for 5 hours in air, display decay profiles that are well-fitted using a bi-exponential model due to the presence of two distinct Cr^{3+} centers within the YAG and YAP lattices. The decay behavior is described by eqn (6):[13,14]

$$I(t) = A_1\tau^{-\frac{t}{\tau_1}} + A_2\tau^{-\frac{t}{\tau_2}} \quad (6)$$

where $I(t)$ is the PL intensity at time t, A_1 and A_2 are constants, and τ_1 and τ_2 are the lifetimes of the respective decay components. The average lifetime (τ) is calculated using eqn (7):[13,14,53]

$$\tau = \frac{A_1\tau_1^2 + A_2\tau_2^2}{A_1\tau_1 + A_2\tau_2} \quad (7)$$

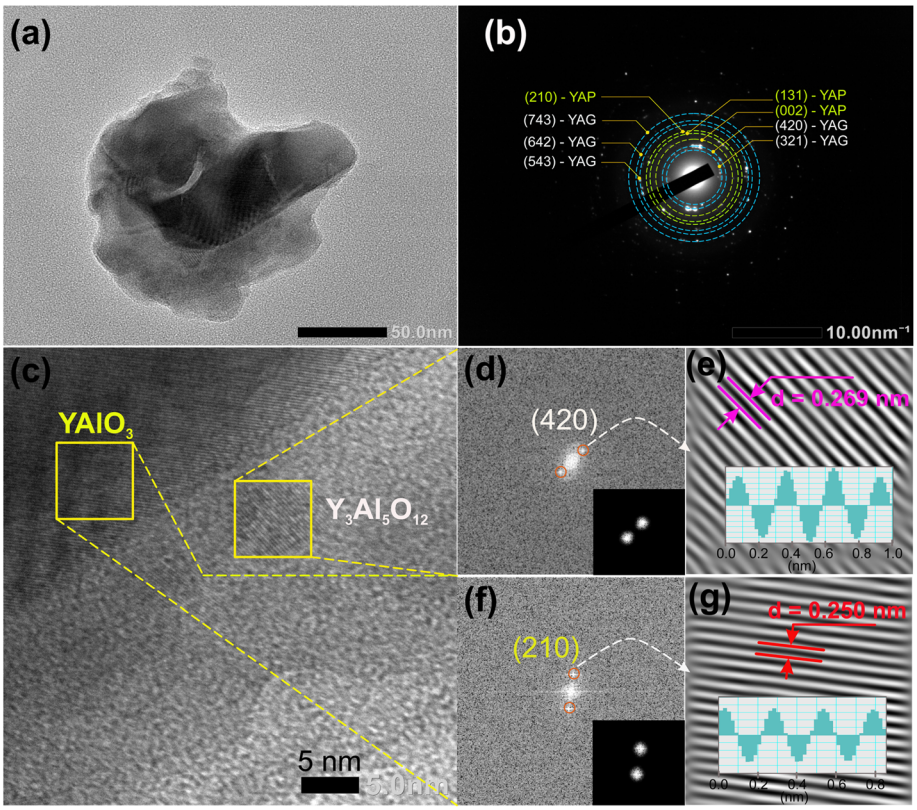

Fig. 4 (a) TEM image, (b) SAED pattern, and (c) high-resolution TEM (HR-TEM) magnified image confirm the coexistence of $Y_3Al_5O_{12}$ and $YAlO_3$ dual-phase structures. (d–g) FFT and IFFT images corresponding to lattice plane fringes of both $Y_3Al_5O_{12}$ và $YAlO_3$ phases.

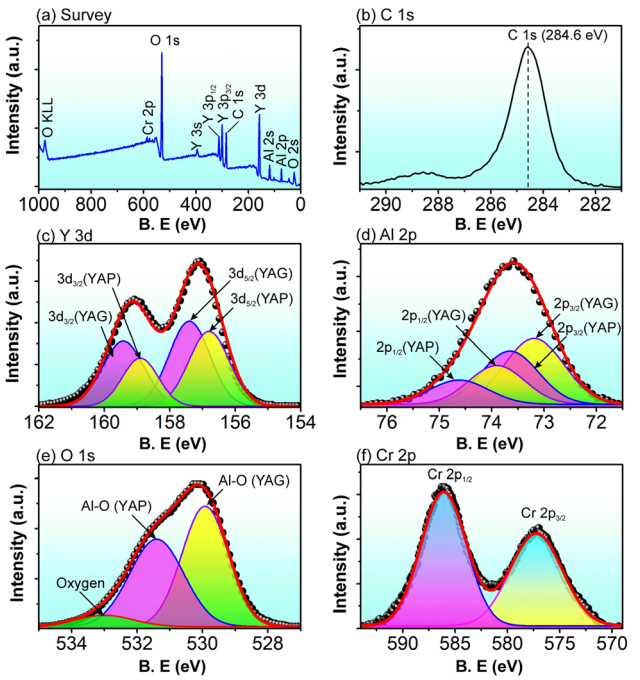

Fig. 5 XPS spectra of $Y_3Al_5O_{12}$–$YAlO_3$:1.3% Cr^{3+} annealed at 1600 °C for 5 h in air: (a) survey, (b) C 1s, (c) Y 3d, (d) Al 2p, (e) O 1s, and (f) Cr 2p.

The corresponding average lifetime values are listed in Table 2. A clear trend is observed: the lifetime decreases from 2.08 ms to 1.81 ms as the Cr^{3+} concentration increases from 0.2% to 1.5%. This reduction is attributed to enhanced energy transfer interactions among closely spaced Cr^{3+} ions at higher doping levels.[13,53]

Thermal stability is a critical parameter for evaluating phosphors performance in LED applications. Fig. 7c presents the PL spectra of the optimized YAG–YAP:1.3% Cr^{3+} phosphors, measured at various temperatures ranging from 30–190 °C. While the spectral shape remains largely unchanged, the emission intensity gradually decreases with increasing temperature. As shown in Fig. S3, the luminescence lifetime of the YAG–YAP:1.3% Cr^{3+} phosphors decreases from 1.86 ms to 1.25 ms, indicating that the reduced emission intensity at elevated temperatures is primarily due to thermally activated non-radiative transitions.[54] The thermal quenching behavior is further illustrated in Fig. 7d and e, where the integrated PL intensity at 150 °C retains approximately 56.2% of its initial value at 30 °C. This retention reflects a thermal stability of 56.2%, outperforming several other Cr^{3+}-doped far-red-emitting phosphors, such as $SrMgAl_{10}O_{17}:Cr^{3+}$ (34.49%),[55] $ScBO_3:Cr^{3+}$ (51%),[56] $Ca_2LuZr_2Al_3O_{12}:Cr^{3+}$ (51.22%).[9] These results confirm the excellent thermal stability of the synthesized phosphors, highlighting their strong potential for LED applications.

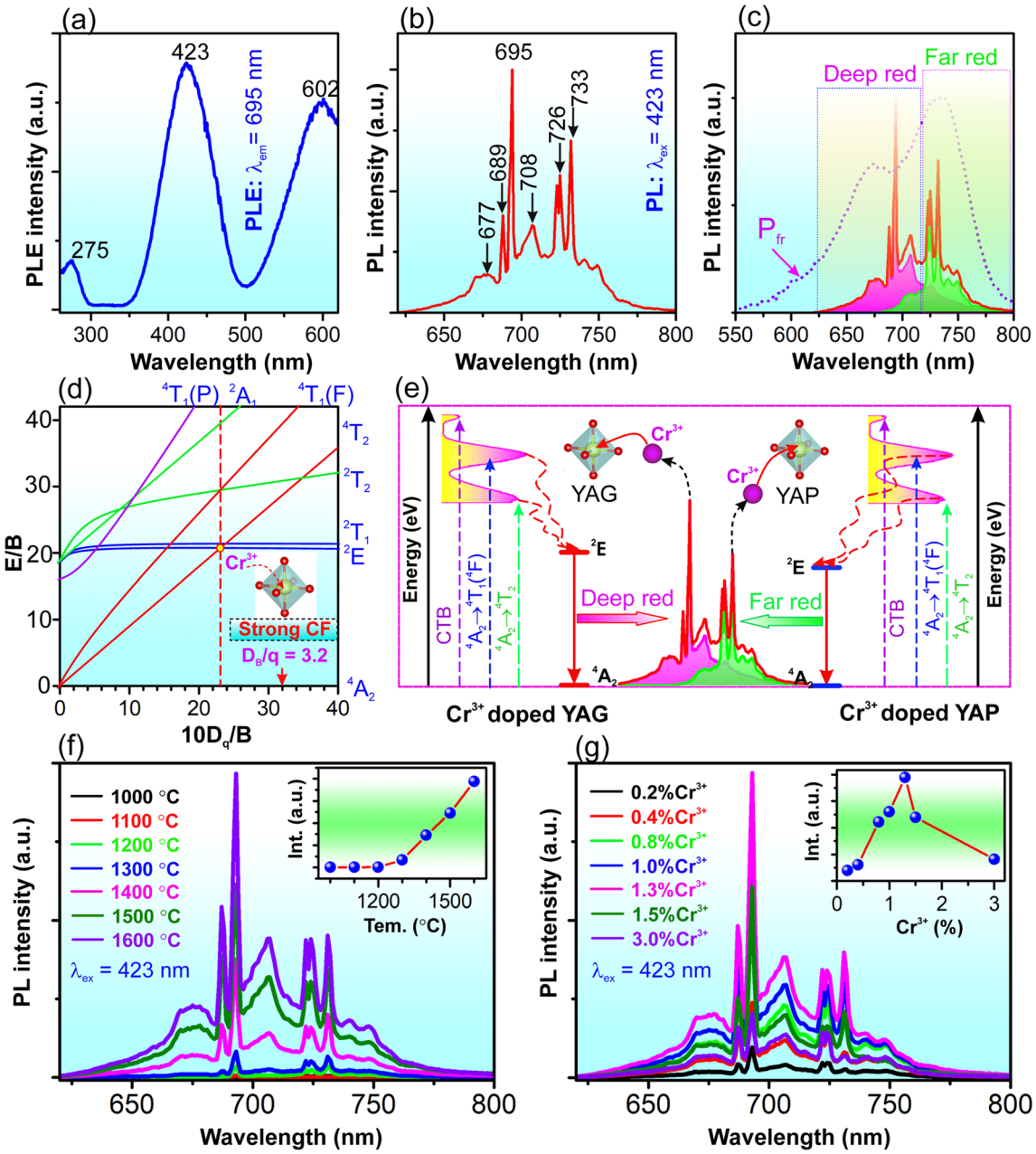

Fig. 6 (a) PLE spectrum and (b & c) PL spectrum and corresponding emission profile are divided into two regions: deep red and far red emissions of the YAG–YAP:1.3% Cr^{3+} sample, (d) Tanabe–Sugano diagram and (e) diagram of energy transitions showcasing the absorption and emission processes in Cr^{3+} doped YAG–YAP phosphors. (f) PL spectra of the YAG–YAP:1.3% Cr^{3+} sample treated at various temperatures and (g) PL spectra of YAG–YAP:*x*% Cr^{3+} ($x = 0.2$–3.0) phosphors synthesized at 1600 °C.

To further assess thermal stability, the activation energy (E_a) of thermal quenching was determined using the Arrhenius eqn (8):[9,55]

$$I = \frac{I_0}{1 + A\mathrm{e}^{\left(-\frac{E_a}{kT}\right)}} \quad (8)$$

This can be linearized as:[9,55]

$$\ln\left(\frac{I_0}{I} - 1\right) = \ln A - \frac{E_a}{kT} \quad (9)$$

where I_0 is the initial PL intensity at room temperature, I is the PL intensity at a given temperature T (in Kelvin), A is a constant, and k is the Boltzmann constant ($k = 8.62 \times 10^{-5}$ eV K^{-1}). The Arrhenius plot of $\ln(I_0/I - 1)$ *versus* $1/T$ is shown in the inset of Fig. 7e. From the slope of the linear fit, the activation energy for the YAG–YAP:1.3% Cr^{3+} phosphor is determined to be approximately 0.34 eV. This value is notably higher than those reported for other Cr^{3+}-doped phosphors, including $SrMgAl_{10}O_{17}:Cr^{3+}$ (0.289 eV),[55] $Ca_2LuZr_2Al_3O_{12}:Cr^{3+}$ (0.073 eV),[9] and $LaSc_{2.9}Y_{0.1}B_4O_{12}:Cr^{3+}$ (0.288 eV),[57] indicating that YAG-YAP:1.3% Cr^{3+} phosphors possess excellent thermal stability. A schematic

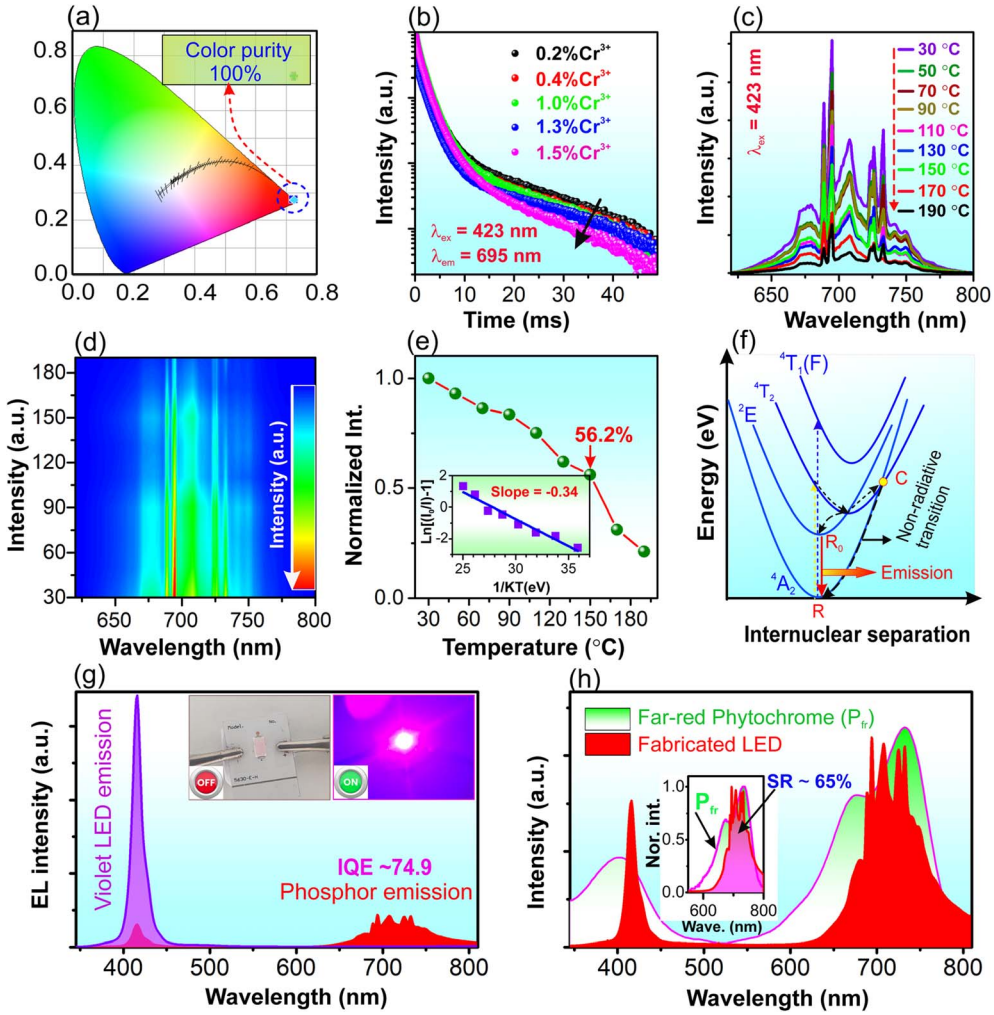

Fig. 7 (a) CIE chromaticity coordinates, (b) lifetime, (c & d) temperature-dependent PL spectra and 3D PL contour mapping spectra, (e) normalized integrated intensity and dependence of $\ln(I_0/I - 1)$ on $1/kT$, (f) illustrative configurational coordinate diagram of YAG–YAP:Cr^{3+}, (g) EL spectra of a 415 nm LED chip before and after phosphor coating, with inset images displaying the fabricated LED in both off and on states, (h) emission spectrum of the fabricated LED with the absorption spectrum of P_{fr}, with the inset displaying the SR index in the far-red region.

illustration of the thermal quenching mechanism is presented in Fig. 7f. Upon excitation at 423 nm, electrons are promoted from the $^4A_2$ ground state to the $^4T_1$ excited state, and subsequently relax to the $^4T_2$ state through non-radiative processes.[50,58] From there, they transition to the long-lived ^2E level, which subsequently decays radiatively to the $^4A_2$ ground state, producing deep-red to far-red emission ($R_0 \rightarrow R$). However, at elevated temperatures, a portion of the excited electrons in the $^4T_2$ state may reach a crossover point (C) between the $^4T_2$ excited state and the $^4A_2$ ground state, allowing non-radiative relaxation directly to the ground state *via* the C → R path.[50] This thermally activated deactivation process accounts for the observed decrease in PL intensity with increasing temperature, as depicted in Fig. 7c.

To demonstrate the practical performance of the far-red phosphor-converted LED, the YAG–YAP:1.3% Cr^{3+} phosphor

Table 2 Color coordinates (x, y), color purity, and average lifetimes at 695 nm of YAG–YAP:x% Cr^{3+} (x = 0.2–1.5) phosphors

Cr^{3+} concentration (% mol)	Chromaticity coordinates (x, y)	Color purity (%)	Lifetime at 695 nm (ms)
0.2	(0.7235, 0.2746)	100	2.08
0.4	(0.7245, 0.2753)	100	2.03
0.8	(0.7257, 0.2742)	100	—
1.0	(0.7256, 0.2743)	100	2.02
1.3	(0.7258, 0.2741)	100	1.86
1.5	(0.7258, 0.2741)	100	1.81
3.0	(0.7260, 0.2739)	100	—

Table 3 Internal quantum efficiency (IQE) of far red-emitting phosphors in previous reports

Phosphors	Emission wavelength (nm)	Excitation wavelength (nm)	Activation energy (eV)	IQE (%)	Ref.
$NaMgLaTeO_6:Mn^{4+}$	703	365	0.255	57.43	36
$K_2Ga_2Sn_6O_{16}:Cr^{3+}$	830	450	—	48.0	60
$K_2NaScF_6:Cr^{3+}$	765	435	—	74.0	61
$ZnGa_2O_4:Cr^{3+}$	710	405	—	52.8	62
$La_2LiSbO_6:Mn^{4+}$, Bi^{3+}	711	491	—	58.71	63
$La_2MgZrO_6:Cr^{3+}$	825	460	0.089	58.0	64
$BaLaZnTaO_6:Mn^{4+}$	695	350	—	16.1	65
$K_2NaInF_6:Cr^{3+}$	774	439	0.306	70.2	66
$CaGdAlO_4:Mn^{4+}$	715	349	—	45.0	67
$Li_6CaLa_2Nb_2O_{12}:Eu^{3+}$	610	393	0.19	65.0	68
$Ca_3La_2W_2O_{12}:Mn^{4+}$	711	360	0.38	47.9	69
$Y_3Al_5O_{12}$–$YAlO_3:Cr^{3+}$	**695 and 733**	**423**	**0.34**	**74.9**	**This work**

was coated onto a violet LED chip (415 nm). The resulting electroluminescence (EL) spectrum, shown in Fig. 7g, displays a broad emission band in the deep red to far-red region (650–800 nm), attributed to the Cr^{3+} emission from the phosphor. Additionally, a sharp peak at 415 nm corresponds to the excitation light from the underlying LED chip. The internal quantum efficiency (IQE) of the phosphor was determined using the following expression:[56–58]

$$\mathrm{IQE} = \frac{\int L_S}{\int E_R - \int E_S} \tag{10}$$

where, $\int L_S$ is the integrated PL spectrum of the YAG–YAP:1.3% Cr^{3+} phosphor. $\int E_S$ and $\int E_R$ represent the integrated PL spectra of the violet LED chip with and without the phosphor coating, respectively.[58] The calculated IQE is approximately 74.9%, which is considered high and superior to many reported Cr^{3+}-doped phosphors, as detailed in Table 3. Fig. 7h compares the emission spectrum of the YAG–YAP:1.3% Cr^{3+} phosphor coated violet LED with the absorption spectrum of phytochrome P_{fr}. To assess spectral compatibility, the overlap ratio in the deep red to far-red region was quantified using the spectrum resemblance (SR) index, defined as follows:[59]

$$\mathrm{SR}_{\text{phytochrome } P_{fr}} = \frac{\int P(\lambda)\mathrm{d}\lambda}{\int P_{\text{phytochrome } P_{fr}}(\lambda)\mathrm{d}\lambda} \times 100\% \tag{11}$$

where, $P(\lambda)$ represents the emission intensity of the phosphor, and $P_{\text{phytochrome } P_{fr}}(\lambda)$ corresponds to the absorption profile of phytochrome P_{fr}. As shown in the inset of Fig. 7h, the calculated SR value is ~65%, indicating a strong spectral match between the phosphor's emission and the absorption of P_{fr}.[58] This significant overlap emphasizes the excellent potential of the YAG–YAP:Cr^{3+} phosphor for plant-targeted LED lighting, particularly in applications aimed at optimizing photomorphogenic responses in plants.

4. Conclusion

$Y_3Al_5O_{12}$–$YAlO_3:Cr^{3+}$ phosphors were successfully synthesized *via* a conventional solid-state reaction method. Structural analysis confirmed that Cr^{3+} ions preferentially occupied the $[AlO_6]$ octahedral sites in both the YAG and YAP lattices, where they experienced strong crystal field effects. Upon excitation at 423 nm, the phosphors exhibited dual emissions in the deep red and far-red spectral regions, with characteristic peaks at 695 nm and 733 nm arising from the spin-forbidden $^2E \rightarrow {}^4A_2$ transition of Cr^{3+} ions in the YAG and YAP hosts, respectively. The optimized $Y_3Al_5O_{12}$–$YAlO_3$:1.3% Cr^{3+} sample, synthesized at 1600 °C for 5 hours in air, demonstrated superior luminescent performance, including a high internal quantum efficiency (IQE) of 74.9%, an activation energy of 0.34 eV, a long photoluminescence (PL) lifetime of 1.86 ms, and a color purity of 100%. To validate its practical application, the optimized phosphor was integrated with a 415 nm violet LED chip to fabricate a far-red pc-LED prototype. These findings underscore the excellent optical properties and thermal robustness of YAG–YAP:Cr^{3+} phosphors, confirming their strong potential for use in plant-targeted LED lighting systems, particularly for applications requiring deep red to far-red spectral output to enhance photomorphogenic responses in horticulture.

Conflicts of interest

The authors declare no conflict of interest.

Data availability

The data supporting this article have been included as part of the SI.

Fig. S1 shows the FTIR spectra of YAG–YAP:x% Cr^{3+} (x = 0.2–3.0) samples annealed at 1600 °C for 5 h in air, confirming the characteristic Al–O and Y–O vibrational bands in the lattice. Fig. S2 presents the photoluminescence excitation (PLE) spectra, which demonstrate that the YAG–YAP:1.3% Cr^{3+} sample annealed at 1600 °C exhibits the highest excitation and emission intensities. As illustrated in Fig. S3, the luminescence lifetime of the YAG–YAP:1.3% Cr^{3+} phosphors decrease from 1.86 ms at 30 °C to 1.25 ms at 190 °C, indicating that the attenuation of emission intensity at elevated temperatures is primarily due to thermally activated nonradiative transitions. Supplementary information is available. See DOI: https://doi.org/10.1039/d5ra03696h.

Acknowledgements

This research is supported by the Ministry of Science and Technology (Vietnam) under Grant No. ĐTĐL.CN-32/2023.

References

1 Y. Zhong, N. Zhou, M. Xia, Y. Zhou, H. Chen and Z. Zhou, *Ceram. Int.*, 2019, **45**, 23528–23539.
2 Y. Han, S. Wang, H. Liu, L. Shi, J. Zhang, Z. Zhang, Z. Mao, D. Wang, Z. Mu, Z. Zhang and Y. Zhao, *J. Lumin.*, 2020, **220**, 116968.
3 L. Sun, B. Devakumar, J. Liang, S. Wang, Q. Sun and X. Huang, *J. Alloys Compd.*, 2019, **785**, 312–319.
4 H. Chen, S. Yan, L. Zhang, B. Zhao, C. Zhu, G. Deng and J. Liu, *Sens. Actuators, B*, 2024, **405**, 135346.
5 Y. Ding, C. Deng, Y. Yang, J. Zhang, W. Liu and O. Aras, *Int. J. Pharm.*, 2025, **671**, 125285.
6 M. T. Tran, D. Q. Trung, N. Tu, D. D. Anh, N. V Du, N. V Quang, N. T. Huyen, D. X. Viet, N. D. Hung and P. T. Huy, *RSC Adv.*, 2021, **884**, 1–13.
7 W. L. Butler, *Annu. Rev. Plant Biol.*, 1964, **16**, 383–392.
8 Z. Zhou, M. Xia, Y. Zhong, S. Gai, S. Huang, Y. Tian, X. Lu and N. Zhou, *J. Mater. Chem. C*, 2017, **5**, 8201–8210.
9 Y. Zheng, H. Zhang, H. Zhang, Z. Xia, Y. Liu, M. S. Molokeev and B. Lei, *J. Mater. Chem. C*, 2018, **6**, 4217–4224.
10 S. Qing, X. Zhang, T. Yang, L. Chu, Y. Zhou, J. Wan, Z. Wang, H. Tang and Q. Zhou, *Dalton Trans.*, 2022, **51**, 16325–16335.
11 M. Li, H. Zhang, X. Zhang, J. Deng, Y. Liu, Z. Xia and B. Lei, *Mater. Res. Bull.*, 2018, **108**, 226–233.
12 Y. Han, L. Shi, H. Liu and Z. Zhang, *Optik*, 2019, **195**, 162014.
13 L. Shi, J. xin Li, Y. jie Han, W. li Li and Z. wei Zhang, *J. Lumin.*, 2019, **208**, 201–207.
14 D. Yu, Y. Zhou, C. Ma, J. H. Melman, K. M. Baroudi, M. Lacapra and R. E. Riman, *ACS Appl. Electron. Mater.*, 2019, **11**, 2325–2333.
15 L. You, R. Tian, T. Zhou and R. Xie, *Chem. Eng. J.*, 2021, **417**, 129224.
16 N. T. Huyen, N. Tu, D. T. Tung, D. Q. Trung, D. D. Anh, T. T. Duc, T. T. T. Nga and T. Huy, *Opt. Mater.*, 2020, **108**, 110207.
17 S. Li, Z. Zhang, J. Zhang, J. Wu, Z. Qiu, M. G. Brik and S. Lian, *Inorg. Chem.*, 2023, **62**, 18740–18749.
18 N. T. Huyen, M. T. Tran, N. V. Quang, H. Q. Bac, D. T. T. Huyen, T. T. K. Nguyet, T. T. Duc, N. D. Hung, D. X. Viet, N. Tu, D. Q. Trung, N. V. Du, D. T. Tung, N. N. Ha and P. T. Huy, *Opt. Mater.*, 2022, **133**, 113002.
19 Y. P. Fu, S. Tsao and C. T. Hu, *J. Alloys Compd.*, 2005, **395**, 227–230.
20 Y. Xu and W. Y. Ching, *Phys. Rev. B: Condens. Matter Mater. Phys.*, 1999, **59**, 530–535.
21 L. Chen, X. Chen, F. Liu, H. Chen, H. Wang, E. Zhao, Y. Jiang, T. S. Chan, C. H. Wang, W. Zhang, Y. Wang and S. Chen, *Sci. Rep.*, 2015, **5**, 1–17.
22 M. Marceddu, M. Manca, P. C. Ricci and A. Anedda, *J. Phys.: Condens. Matter*, 2012, **24**, 135401.
23 L. Marciniak, A. Bednarkiewicz, J. Drabik, K. Trejgis and W. Strek, *Phys. Chem. Chem. Phys.*, 2017, **19**, 7343–7351.
24 T. Xu, L. Yuan, Y. Chen, Y. Zhao, L. Ding, J. Liu, W. Xiang and X. Liang, *Opt. Mater.*, 2019, **91**, 30–34.
25 P. Głuchowski, R. Pązik, D. Hreniak and W. Stręk, *J. Lumin.*, 2009, **129**, 548–553.
26 K. K. Kumarbekov, Z. S. Zhilgildinov, Z. T. Karipbayev, A. M. Zhunusbekov, E. E. Nurmoldin, M. G. Brik, Y. Suchikova, M. Kemere, A. I. Popov and M. T. Kassymzhanov, *Opt. Mater.*, 2025, **159**, 116535.
27 L. Shao and X. Jing, *J. Lumin.*, 2011, **131**, 1216–1221.
28 A. A. Kravtsov, V. A. Tarala, F. F. Malyavin, D. S. Vakalov, V. E. Suprunchuk, L. V Tarala, V. A. Lapin, E. V Medyanik, E. A. Brazhko and O. M. Chapura, *J. Eur. Ceram. Soc.*, 2023, **43**, 7085–7095.
29 J. A. Mares, W. Nie and G. Boulon, *J. Phys.*, 1990, **51**, 1655–1669.
30 M. J. Weber and T. E. Varitimos, *J. Appl. Phys.*, 1974, **45**, 810–816.
31 M. T. Tran, N. Tu, N. V Quang, D. H. Nguyen, L. T. H. Thu, D. Q. Trung and P. T. Huy, *J. Alloys Compd.*, 2021, **853**, 156941.
32 M. Skruodiene, M. Misevicius, M. Sakalauskaite, A. Katelnikovas and R. Skaudzius, *J. Lumin.*, 2016, **179**, 355–360.
33 M. Skruodiene, A. Katelnikovas, L. Vasylechko and R. Skaudzius, *J. Lumin.*, 2019, **208**, 327–333.
34 A. Suzuki, S. Kurosawa, A. Yamaji, Y. Shoji, J. Pejchal, K. Kamada, Y. Yokota and A. Yoshikawa, *Opt. Mater.*, 2014, **36**, 1938–1941.
35 K. Li, H. Lian, R. Van Deun and M. G. Brik, *Dyes Pigm.*, 2019, **162**, 214–221.
36 K. Li, H. Lian, R. Van Deum and M. G. Brik, *Dyes Pigments*, 2019, **162**, 214–221.
37 M. K. Husen and F. B. Dejene, *J. Sol-Gel Sci. Technol.*, 2018, **88**, 454–464.
38 Y. Kang, S. Li, R. Tian, G. Liu, H. Dong, T. Zhou and R. J. Xie, *J. Adv. Ceram.*, 2022, **11**, 1383–1390.
39 G. Dong, X. Xiao, Y. Chi, B. Qian, X. Liu, Z. Ma, E. Wu, H. Zeng, D. Chen and J. Qiu, *J. Chem. C*, 2010, **20**, 1587–1593.
40 P. Palmero and C. Esnouf, *J. Eur. Ceram. Soc.*, 2011, **31**, 507–516.
41 M. Szubka, E. K. Talik, J. Kusz, H. Sakowska and M. Świrkowicz, *Acta Phys. Pol., A*, 2009, **115**, 209–212.
42 D. M. Kim, S. H. Lee, W. B. Alexander, K. B. Kim, Y. S. Oh and S. M. Lee, *J. Am. Ceram. Soc.*, 2011, **94**, 3455–3459.
43 H. B. Premkumar, H. Nagabhushana, S. C. Sharma, S. C. Prashantha, H. P. Nagaswarupa, B. M. Nagabhushana and R. P. S. Chakradhar, *J. Alloys Compd.*, 2014, **601**, 75–84.
44 R. T. Haasch, E. Breckenfeld and L. W. Martin, *Surf. Sci. Spectra*, 2014, **21**, 95–102.
45 T. Xu, L. Yuan, Y. Chen, Y. Zhao, L. Ding, J. Liu, W. Xiang and X. Liang, *Opt. Mater.*, 2019, **91**, 30–34.
46 B. M. Małysa, PhD thesis, Utrecht University, 2019.
47 Z. Liu, X. Yu, Q. Peng, X. Zhu, J. Xiao, J. Xu, S. Jiang, J. Qiu and X. Xu, *Adv. Funct. Mater.*, 2023, **33**, 2214497.

48 C. Chen, J. Wang, S. Bi, Y. Huang and H. Jin, *J. Alloys Compd.*, 2019, **786**, 1051–1059.
49 T. Tan, S. Wang, J. Su, W. Yuan, H. Wu, R. Pang, J. Wang, C. Li and H. Zhang, *ACS Sustain. Chem. Eng.*, 2022, **10**, 3839–3850.
50 K. T. Thu, N. Tu, D. Q. Quang, N. V. Du, M. T. Trung, N. V. Quang, T. N. Bach, N. T. H. Lien, N. D. Hung, D. X. Viet, N. D. T. Kien and P. T. Huy, *Ceram. Int.*, 2024, **50**, 27064–27079.
51 B. S. Ravikumar, H. Nagabhushana, S. C. Sharma, Y. S. Vidya and K. S. Anantharaju, *Spectrochim. Acta, Part A*, 2015, **136**, 1027–1037.
52 R. Naik, S. C. Prashantha, H. Nagabhushana, S. C. Sharma, H. P. Nagaswarupa and K. M. Girish, *J. Alloys Compd.*, 2016, **682**, 815–824.
53 Q. Sun, S. Wang, B. Devakumar, L. Sun and J. Liang, *RSC Adv.*, 2019, **9**, 3303–3310.
54 F. Zhu, Y. Gao and J. Qiu, *ACS Appl. Mater. Interfaces*, 2024, **16**, 60599–60607.
55 Y. Han, L. Shi, H. Liu and Z. Zhang, *Optik*, 2019, **195**, 162014.
56 Q. Shao, H. Ding, L. Yao, J. Xu, C. Liang and J. Jiang, *RSC Adv.*, 2018, **8**, 12035–12042.
57 T. Gao, W. Zhuang, R. Liu, Y. Liu, X. Chen and Y. Xue, *J. Alloys Compd.*, 2020, **848**, 156557.
58 S. J. Gai, C. Zhou, L. Peng, M. H. Wu, P. X. Gao, L. J. Su, M. S. Molokeev, Z. Zhou and M. Xia, *Mater. Today Chem.*, 2022, **26**, 101107.
59 J. Jou, C. Lin, T. Li, C. Li, S. Peng, F. Yang, K. R. J. Thomas, D. Kumar, Y. Chi and B. Hsu, *Materials*, 2015, **162**, 5265–5275.
60 J. Lai, W. Shen, J. Qiu, D. Zhou, Z. Long, Y. Yang, K. Zhang, I. Khan and Q. Wang, *J. Am. Ceram. Soc.*, 2020, **103**, 5067–5075.
61 E. Song, H. Ming, Y. Zhou, F. He, J. Wu, Z. Xia and Q. Zhang, *Laser Photonics Rev.*, 2021, **15**, 1–8.
62 M. Li, H. Zhang, X. Zhang, J. Deng, Y. Liu, Z. Xia and B. Lei, *Mater. Res. Bull.*, 2018, **108**, 226–233.
63 Y. Zhang, S. Sun, P. Yin, Y. Yang, L. Fu, J. Wang, X. Feng, H. Rao and Y. Wang, *J. Lumin.*, 2020, **224**, 117268.
64 H. Zeng, T. Zhou, L. Wang and R. J. Xie, *Chem. Mater.*, 2019, **31**, 5245–5253.
65 Y. Lan, Z. Sun, Z. Lu, C. Liang and L. Zhou, *Opt. Laser Technol.*, 2019, **119**, 105614.
66 Z. Wu, X. Han, Y. Zhou, K. Xing, S. Cao, L. Chen, R. Zeng, J. Zhao and B. Zou, *Chem. Eng. J.*, 2022, **427**, 131740.
67 Q. Sun, S. Wang, B. Li, H. Guo and X. Huang, *J. Lumin.*, 2018, **203**, 371–375.
68 P. Du, Q. Meng, X. Wang, Q. Zhu, X. Li, X. Sun and J. G. Li, *Chem. Eng. J.*, 2019, **375**, 121937.
69 X. Huang and H. Guo, *Dyes Pigm.*, 2018, **152**, 36–42.